Full length article

Three-dimensional CFD-DEM simulation of raceway transport phenomena in a blast furnace

Navid Aminnia [a,*], Prasad Adhav [a], Fateme Darlik [a], Muhammad Mashhood [a], Sina Hassanzadeh Saraei [a], Xavier Besseron [a], Bernhard Peters [a]

[a] University of Luxembourg, Department of Engineering, Maison du Nombre, 6 Avenue de la Fonte, L-4364, Esch-sur-Alzette, Luxembourg

ARTICLE INFO

ABSTRACT

Improving energy efficiency in a blast furnace (BF) has a significant effect on energy consumption and pollutant emission in a steel plant. In the BF, the blast injection creates a cavity, the so-called raceway, near the inlet. On the periphery of the raceway, a ring-type zone is formed which is associated with the highest coke combustion rate and temperatures in the raceway. Therefore, predicting the raceway size or in other words, the periphery of the ring-type zone with accuracy is important for estimating the BF's energy and coke consumption. In the present study, Computational Fluid Dynamics (CFD) is coupled to Discrete Element Method (DEM) to develop a three-dimensional (3D) model featuring a gas–solid reacting flow, to study the transport phenomena inside the raceway. The model is compared to a previously developed two-dimensional (2D) model and it is shown that the assumptions associated with a 2D model, result in an overestimation of the size of the raceway. The 3D model is then used to investigate the coke particles' combustion and heat generation and distribution in the raceway. It is shown that a higher blast flow rate is associated with a higher reaction rate and a larger raceway. A 10% increase in the inlet velocity (from 200 m/s to 220 m/s) caused the raceway volume to grow by almost 40%. The DEM model considers a radial discretization over the particle, therefore the heat and mass distributions over the particle are analyzed as well.

1. Introduction

The ironmaking industry produces 7% of the world's total carbon dioxide emissions [1]. The most frequent ironmaking process is the blast furnace (BF), accounting for more than 70% of total energy consumption in the ironmaking industry [2] and 90% of the CO2 emission [3]. As a result, lowering energy usage and gas pollution in the BF ironmaking operations has received a lot of attention [4].

The region inside the furnace which is created by injecting hot blast air into the coke bed is called the raceway. Its shape is affected by different parameters such as blast velocity, the geometry of the nozzles, and operational circumstances [5]. Therefore, the study of the raceway is vital to analyze the gas species distributions and heat supplies which, directly have an impact on the furnace's productivity and efficiency. As a result, the raceway has been comprehensively studied, especially the principles of the particle scale. Experimental and computational methods have been used extensively to study raceway phenomena over the past few decades. As a consequence of the severe operating circumstances within the actual BF process (e.g., high temperature and

pressure situations), measurement during an experimental test is difficult to undertake and only a few studies have worked on this with very limited data, such as gas species distributions [6]. For example, Matsui et al. [7] used microwave reflection gunned via a tuyere to study the BF raceway formation under heavy coal injection rate circumstances. Sastry et al. [8] studied the particle system in a two-dimensional (2D) cold model. In another study, Sastry et al. [9] conducted experimental research in a packed bed and found that the characteristics of coke particles had a significant impact on cavity development and breakdown. Zhang et al. [10] used an image-based flame detection approach to investigate the combustion characteristics of a BF raceway and discovered that the raceway temperature profile could fluctuate considerably. These experimental studies despite helping us gain a better picture of how raceways work can only explain BF functioning at the macro-scale information such as pressure and temperature in the local spots and are not able to obtain the micro-scale information such as inter-particle/phase interactions, raceway shape/size, heat transfer, coke combustion.

Nomenclature

Physical constants/Greek symbols

α	Heat transfer coefficient (W/(m^2 K))
β	Interphase momentum exchange (kg/(m^3 s))
ϵ	Porosity (-)
λ_f	Thermal conductivity (W/(m K))
μ	Dynamic viscosity (Pa s)
η	Weight of particle for porosity calculation (-)
Ω_c	Implicitly treated drag term (1/s)
ρ	Density (kg/m^3)

Operators

∂	Differential operator (–)
Δ	Difference (–)
∇	Nabla operator (–)

Scalars

A	Surface Area (m^2)
c_p	Specific Heat (J/kg K)
C_d	Drag Coefficient (–)
d	Particle diameter (m)
h	Convective heat transfer coefficient (W/(m^2 K))
I_i	Moment of inertia (kg m^2)
m	Mass (kg)
m'	Mass source (kg/(m^3 s))
p	Pressure (Pa)
q'	Heat source (W/m^2)
q''	Heat flux (W/m^2)
r, R	Radius (m)
Re	Reynolds number (–)
t	Time (s)
T	Temperature (K)
T_{final}	Length of simulation (s)
V	Volume (m^3)

Subscripts

c	Cell
$cond$	Conduction
d	Drag
eff	Effective values
f	Fluid
i, j	Particle
n	Normal direction
p, P	Particle
s	Solid
rad	Radiation
t	Tangential direction

Superscripts

n	Geometry exponent
(n)	nth (time) step
$(n + 1)$	nth (time) step +1

First order tensors (vectors)

$\vec{A}_c$	Acceleration on fluid cell due to explicitly treated drag term (m/s^2)
$\vec{g}$	Gravitational acceleration (m/s)
$\vec{F^c}$	Contact Forces (N)
$\vec{F^g}$	Gravitational Force (N)
$\vec{F^{ext}}$	External Forces (N)
$\vec{F}_B$	Buoyancy Force (N)
$\vec{F}_D$	Drag Force (N)
$\vec{M}_{i,j}$	Torque generated by inter-particle forces (N m)
$\vec{v}_f$	Fluid velocity field
$\vec{X}_i$	Positional vector (m)
$\vec{\omega}$	Rotational velocity (rad/s)

In light of the limitations of experimental research and the difficulty of performing accurate measurements, numerical simulations are generally employed to study raceway phenomena. Numerical simulations are divided into two common categories: Eulerian–Eulerian and Eulerian–Lagrangian. Mondal et al. [11] studied the influences of the air blast velocity on the shape and size of the raceway zone in a BF by using the Eulerian–Eulerian model. However, the Eulerian–Eulerian model has no capacity of obtaining information such as particle and phase interactions, particle residence time, and particle trajectory [12]. Besides the simple assumptions of inter-particle collisions in this method make it difficult to adequately capture numerous interparticle collisions near the tuyere and the quasi-static-regime in the deadman region and the associated flow features [13]. Such difficulties can be overcome by one of the important Eulerian–Lagrangian methods, the discrete element method (DEM) coupled with Computational Fluid Dynamics (CFD) named CFD-DEM. In recent years, many studies have applied CFD-DEM methods to investigate the raceway's information. For example, Xu et al. [14] proposed CFD-DEM methods to study gas fluidization on fixed and fluidized beds. To comprehend raceway formation, they illustrated that this method can capture gas–solid flow characteristics ranging from large scale (such as processing equipment) to little scale features (such as each particle). Feng et al. [15] developed a 2-dimensional model to study the particle flow in the modeling of BF, finding that both solid and gas phases flow are changed spatially and temporally, in particular in the cohesive zone, which is affected by the layered ore and coke particle structure. Yuu et al. [16] compared the characteristics of the raceway such as depth and heights with experimental data and additionally reported dynamic characteristics such as the flow of solid particles, and the airflow around the raceway. Hilton and Cleary [17] used a discrete approach and observed the effect of injection velocity and bed pressure on the formation of raceway and investigate those non-spherical particles, as opposed to spherical particles, can form the raceways at higher gas input velocities. Wang and Shen [18] developed a reacting model to study raceway formation at the particle scale and discussed the impacts of several factors on raceway combustion (such as inlet velocity, temperature, and oxygen mass fraction). To examine raceway formation, Miao et al. [19] published a 2D CFD-DEM model for full-scale BF conditions and showed that in comparison to the studies in the laboratory circumstance, the raceway parameters are substantially more complicated in full-scale BF. Cui et al. [20] used a particle scale CFD-DEM method to study the raceway cavity shape and its parameters such as heat source, mass source, and chemical reactions and additionally the effect of the gas inlet velocity, size of particles, and particle discharge rate on the raceway formation. Dianyu et al. [21] also developed a 2D CFD-DEM model to analyze the effect of parameters such as particle size and oxygen enrichment on raceway formation and gasification rate. Recently, there has been an increasing interest in operating furnaces using renewable fuels, such as hydrogen, and many researchers have used CFD simulations to prove their efficiency [22–24]. Though this study does not consider renewable fuels, its findings can be applied to such endeavors.

The present study emphasizes the superior ability of 3D models over 2D models to predict the behavior of raceways. Therefore a 3D particle-scale CFD-DEM model of a BF raceway is developed. Using radial discretization, heat and mass transfers within particles are solved, therefore the internal gradients of particles are seen. The developed model incorporates oxidation reactions within the particles and heat and mass transfer between particles and the gas. Additionally, the impact of parameters such as inlet velocity and particle mesh on raceway size and temperature distribution is discussed. In Section 2 the governing equations of CFD and DEM models are presented along with the details of coupling techniques. In Section 3 the results of the validation of the 3D model is presented. Then, using the comparisons between the 2D and 3D models it is argued that the inherent assumptions associated with 2D models make it unable to predict the raceway dynamics with precision. In the same section the results from the 3D model are presented and discussed. It is also shown that the discretization of the particles in the DEM model can have significant effect on the predicted size of the raceway and the gas temperature.

2. Model description

XDEM software [25] is used in the current work. This software uses Eulerian-Lagrangian approach to for CFD-DEM coupling. Its multi-scale and multi-physics framework considers particles as discrete entities while fluid as a continuous medium.

2.1. Governing equations for discrete particles

XDEM predicts both dynamics and thermodynamics of the particulate system. The particle position, velocity and acceleration are calculated with the dynamics module of the XDEM, where as the temperature, and processes like combustion, gasification, drying etc are calculated with the conversion module of the XDEM.

2.1.1. Dynamics module

The Discrete Element Method (DEM) used in the dynamics module of XDEM is based on the soft sphere model. In this method, it is assumed that the particles are deformable and can overlap each other, where the magnitude of overlap is decided by the contact force using the force–displacement law. The hardness of the particle is expressed via Young's Modulus, while the particle energy dissipation is described with dampener and/or dashpot. The translational and rotational movements of individual particles are tracked using the classical mechanics equations. A detailed description of all the terms mentioned below could be found in previous work [26]. A summary of the translational and rotational motion equations is given below: Equations of particle motion:

$$m_i \frac{d\vec{v}_i}{dt} = m_i \frac{d^2 \vec{X}_i}{dt^2} = \vec{F}_i^c + \vec{F}_i^g + \vec{F}_i^{ext} \tag{2.1}$$

where $\vec{F}_i^{ext}$ is the sum of all the external forces acting on the particle, such as buoyancy forces $\vec{F}_B$ (Eq. (2.25)) and drag forces $\vec{F}_D$ (Eq. (2.26)).

$$I_i \frac{d\vec{\omega}_i}{dt} = \sum_{j=1}^{n} \vec{M}_{i,j} \tag{2.2}$$

2.1.2. Conversion module

The particles a modeled with pores/voids. These pores are modeled to have a gaseous mixture of different chemical species. Mass conservation equation for fluid within particles pores:

$$\frac{\partial}{\partial t} \left(\epsilon_f \rho_f \right) + \vec{\nabla} \cdot \left(\epsilon_f \rho_f \vec{v}_f \right) = m'_{s,f} \tag{2.3}$$

One dimensional transient energy conservation equations for particles:

$$\frac{\partial \rho c_p T}{\partial t} = \frac{1}{r_n} \frac{\partial}{\partial r} \left(r^n \lambda_{eff} \frac{\partial T}{\partial r} \right) - r^n \left(\vec{v}_f \rho_f c_{p_f} T \right) + \sum_{k=1}^{l} \dot{\omega}_k H_k \tag{2.4}$$

The mass balance and transport equation of individual fluid species within the particle pores:

$$\frac{\partial}{\partial t} \left(\epsilon_f \rho_{f,i} \right) + \nabla \cdot \left(\epsilon_f \rho_{f,i} \cdot \vec{v}_f \right) = \frac{1}{r_n} \frac{\partial}{\partial r} \left(r^n \epsilon_f D \frac{\partial \rho_{f,i}}{\partial t} \right) + m'_{s,f,i} \tag{2.5}$$

Following boundary conditions are applicable to the governing equations mentioned above:

$$-\lambda_{eff} \frac{\partial T}{\partial r} \bigg|_{r=0} = 0 \tag{2.6}$$

$$-\lambda_{eff} \frac{\partial T}{\partial r} \bigg|_{r=R} = \alpha(T_R - T_\infty) + q''_{rad} + q''_{cond} \tag{2.7}$$

$$- D_{i,eff} \frac{\partial \rho_i}{\partial r} \bigg|_{r=R} = \beta_i \left(\rho_{i,R} - \rho_{i,\infty} \right) \tag{2.8}$$

In Eq. (2.7), q''_{cond} and q''_{rad} are conduction and radiation heat source respectively from the neighboring particles. The detailed description of the conduction and radiation between particles is given in B. Peters [27].

In the conversion module of XDEM, a radial discretization is considered to solve for heat & mass transfer within the particle. This radial discretization can be uniform or non-uniform, as shown in Fig. 1. In the current work, non-uniform radial discretization is utilized. The non-uniform radial discretization allows to have smaller cell length near the particle surface that allows the model to capture the sharp temperature and mass flow gradients.

2.2. Governing equations for fluid

In Eulerian volumetric average method, the conservation equation of mass (Eq. (2.10)), momentum (Eq. (2.11)) and energy (Eq. (2.12)) are written over a representative volume, where porosity (ϵ Eq. (2.9)) refers to the interstitial solid space particles. These governing equations for fluids are given below. Detailed description of the porosity calculation can be found in [26], the porosity calculation in brief is as follows, where V_c is CFD cell volume, V_i is the particle volume of ith particle in the CFD cell and η is weight for porosity calculation:

$$\epsilon = 1 - \frac{1}{V_c} \sum_{i}^{n} \eta_i V_i \tag{2.9}$$

Conservation of mass

$$\frac{\partial}{\partial t} \left(\epsilon \rho_f \right) + \nabla \cdot \left(\epsilon \rho_f \vec{v}_f \right) = m' \tag{2.10}$$

Conservation of momentum

$$\frac{\partial}{\partial t} \left(\epsilon \rho_f \vec{v}_f \right) + \nabla \cdot \left(\epsilon \rho_f \vec{v}_f \vec{v}_f \right) = -\epsilon \nabla p + \epsilon \rho_f \vec{g} + \epsilon \rho_f \vec{A}_c + \epsilon \mu \nabla^2 \vec{v}_f - \epsilon \rho_f \Omega_c \vec{v}_{f_c} \tag{2.11}$$

Conservation of energy

$$\frac{\partial}{\partial t} \left(\epsilon \rho_f h_f \right) + \nabla \cdot \left(\epsilon \rho_f \vec{v}_f h_f \right) = \frac{\partial p}{\partial t} + \epsilon \vec{v}_f \cdot \nabla p + q' \tag{2.12}$$

Chemical reactions are also considered in the CFD solver. In a multispecies gas mixture, the mass conservation equation for a species i, is given in Eq. (2.13):

$$\frac{\partial}{\partial t} \epsilon \rho_{f,i} + \nabla \cdot \left(\epsilon \rho_{f,i} \cdot \vec{v}_f \right) = m'_i \tag{2.13}$$

2.3. Chemical reactions

The current study focuses on the raceway and areas immediately next to raceway. In this region mainly gasification and combustion reactions are observed in the particles, the (solid phase) reactions are presented in Eqs. (2.14), (2.15), and (2.16). Considering the temperatures in and near raceway, the reaction (2.14) producing CO is mainly observed. Some small amount CO_2 is produced as shown in reaction
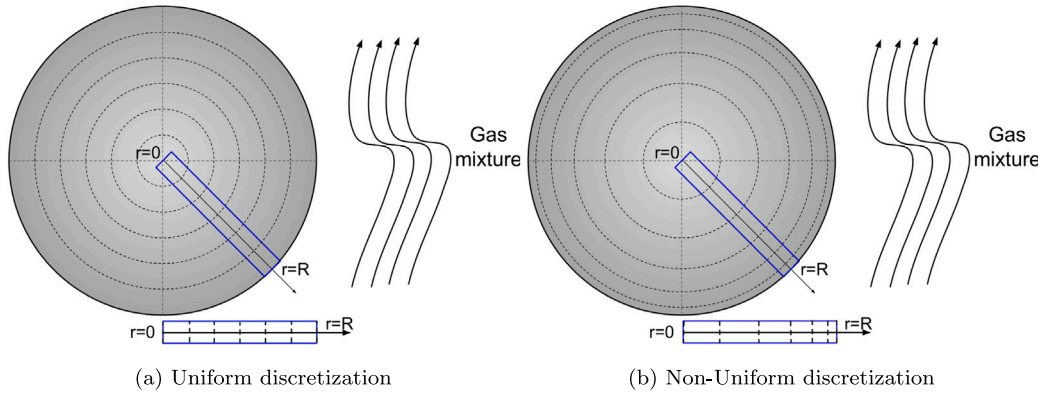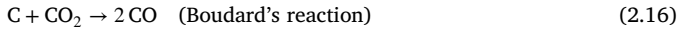
(a) Uniform discretization   (b) Non-Uniform discretization

Fig. 1. Radial discretization for heat & mass transfer within a particle.

(2.15), but due to high temperatures ($\geq$1073 K [28]) it quickly decomposes to CO as shown in gas phase reaction (2.16). The gasification reactions are as follows:

$$C + 0.5\,O_2 \rightarrow CO \tag{2.14}$$

$$C + O_2 \rightarrow CO_2 \tag{2.15}$$

$$C + CO_2 \rightarrow 2\,CO \quad \text{(Boudard's reaction)} \tag{2.16}$$

As opposed to the previous reactions, reaction (2.17) is taking place in purely gaseous state (handled by CFD solver). Due to the high temperatures in the region of interest, it is observed that the CO_2 produced from the following chemical reactions, converts back to CO according to reaction (2.16).

$$CO + 0.5\,O_2 \rightarrow CO_2 \tag{2.17}$$

Generally reactions can be written as follows:

$$\sum_{i=1}^{N} v_i'\, R_i \; \rightleftharpoons \; \sum_{j=1}^{M} v_j''\, P_j \tag{2.18}$$

where N denotes the number of reactants R_i, M denotes the number of products P_j and $v_{i/j}$ represents the absolute values of the corresponding stoichiometric coefficient.

$$\dot{\omega} = -\frac{1}{v_i'}\frac{dc_i}{dt} = \frac{1}{v_j''}\frac{dc_j}{dt} \tag{2.19}$$

The actual reaction rate $\dot{\omega}$ may depend on species concentrations, the available reactive surface O_{sp} and the temperature; so that in general $\dot{\omega} = f(c_i, c_j, O_{sp}, T, \ldots)$. Thus, an Arrhenius law is employed to describe the temperature dependency of the reaction rate as

$$k(T) = k_0\, e^{\left(\frac{-E_a}{RT}\right)} \tag{2.20}$$

where $k(T)$ represents the temperature dependent rate coefficient, k_0 referred to as frequency factor and E_a denotes the activation energy.

If thermodynamic equilibrium is reached, then an equilibrium constant $K_{eq,c}$, representing the thermodynamically equilibrium state, can be obtained as

$$K_{eq,c}(T) = \frac{k_f(T)}{k_b(T)} = \frac{\prod_{j=1}^{M} c_{eq,P_j}^{v_j''}}{\prod_{i=1}^{N} c_{eq,R_i}^{v_i'}} \tag{2.21}$$

In the XDEM software, the equilibrium constant $K_{eq,c}(T)$ is calculated as

$$K_{eq,c}(T) = e^{\frac{A_{eq}}{T} + B_{eq}} \tag{2.22}$$

where A_{eq} and B_{eq} are constant values that may come from existing tables or from equilibrium diagrams of phase diagrams (see Table 1).

Table 1
Chemical reaction rates.

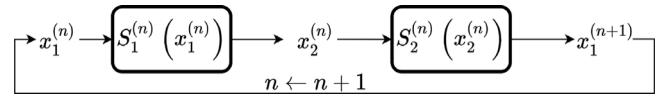| Variable	Reaction (2.14)	Reaction (2.17)
E_a	149,000	20,129
A_{eq}	0	2.24e+08
B_{eq}	0	0
Temperature range	273 K to 1500 K	273 K to 1500 K

Fig. 2. Serial staggered coupling scheme.

2.4. CFD-DEM coupling

The CFD-DEM coupling is achieved through conventional staggered approach. In this approach, the output from one simulation (solver) is used as an input for the other. Considering current work, assume that solver S_1 is the CFD solver, and the solver S_2 is DEM solver. The fluid solver S_1 solves the momentum, mass, reactions and energy equations for the fluid. The fluid solver output such as the fluid velocity, temperature, species mass fraction etc., are then used as boundary conditions for the particles in DEM solver S_2. The DEM solver S_2 uses solution from CFD solver, to compute various source terms by computing the momentum and energy equations for particles. In the next time step, these source terms are communicated to the fluid solver S_1, which then uses the solution from nth time step to get a new solution for the $(n+1)$ time step.

$$x_2^{(n+1)} = S_1^{(n)}\left(x_1^{(n)}\right) \tag{2.23}$$

In Eq. (2.23), CFD solver S_1 uses old time step's boundary value (or in case of first time step it can be the boundary conditions or an initial guess), $x_1^{(n)}$ to compute the values of x_2 for next time step $x_2^{(n+1)}$. During this time, DEM solver S_2 waits for CFD solver S_1 to compute solution and exchange the updated solution $x_2^{(n+1)}$.

$$x_1^{(n+1)} = S_2^{(n)}\left(x_2^{(n+1)}\right) \tag{2.24}$$

In Eq. (2.24), the updated solution x_2 is used to update the solution for x_1 for the next time step. This can also be seen graphically in Fig. 2.

2.4.1. Fluid forces on particles

There are two types of fluid forces acting on the particles, namely hydrostatic force and hydrodynamic force. The hydrostatic force is the

buoyancy force which accounts for the pressure gradient around an individual particle [29].

$$\vec{F}_B = -V_{p_i} \nabla p \tag{2.25}$$

In the Eulerian–Lagrangian approach, the hydrodynamic force corresponds to the fluid–particle interaction. This force depends on the relative velocity of the solid particle and fluid along with the forces acting due to presence of neighboring particles. The drag force acting on the particle due the fluid for CFD-DEM approach is given as follows:

$$\vec{F}_{\vec{D}} = \frac{\beta V_p}{(1-\epsilon)} \left(\vec{v}_f - \vec{v}_p \right) \tag{2.26}$$

The interphase momentum exchange β is predicted according to Gidaspow [30]. Although to cover all range of void fraction (ϵ), Wen and Yu [31] ($\epsilon \geq 0.8$) and Ergun and Orning [32] ($\epsilon < 0.8$) equations are included.

$$\beta = \begin{cases} 150\dfrac{(1-\epsilon)^2}{\epsilon}\dfrac{\mu_f}{d_p^2} + 1.75(1-\epsilon)\dfrac{\rho_f}{d_p}|\vec{v}_f - \vec{v}_p|, & \text{if} \quad \epsilon < 0.8 \\ \dfrac{3}{2}C_d\dfrac{\epsilon(1-\epsilon)^2}{d_p}\rho_f|\vec{v}_f - \vec{v}_p|\epsilon^{-2.65}, & \text{if} \quad \epsilon \geq 0.8 \end{cases} \tag{2.27}$$

where the drag coefficient C_d is given as:

$$C_d = \begin{cases} \dfrac{24}{Re}\left[1 + 0.15(Re)^{0.687}\right], & \text{if} \quad Re < 1000 \\ 0.44, & \text{if} \quad Re \geq 1000 \end{cases} \tag{2.28}$$

and the Reynolds number for the particle is given as:

$$Re = \frac{\epsilon \rho_f |\vec{v}_f - \vec{v}_p| d_p}{\mu_f} \tag{2.29}$$

2.4.2. Particle momentum source terms

In the fluid, the drag exerted by the solid particles is treated in semi-implicit way according to the method proposed by Xiao and Sun [33]. The explicit momentum source term $\vec{A}_c$ and implicit momentum source term Ω_c are as given in Eq. (2.30)

$$\vec{A}_c = \frac{1}{\rho_f V_c}\widetilde{\sum_i} B_i \vec{u}_{p_i}, \quad \Omega_c = \frac{1}{\rho_f V_c}\sum_{i=1}^{c_n} B_i \tag{2.30}$$

2.4.3. Particle heat and mass source terms

Fluid flow conditions such as fluid temperature, specific heat, thermal conductivity, species mass fractions are exchanged from CFD to DEM. These are used as boundary conditions for solving energy balance, mass balance and reaction equations for particles.

Based on the energy balance equations, heat loss/gain due convection or due to change in composition of particles is computed. This is used as the (explicit) heat source in fluid energy equation. Similarly, mass source and species mass fraction source are computed.

$$q_i' = h_i A_i (T_{p_i} - T_f) \tag{2.31}$$

where h_i is the heat transfer coefficient for a given particle i, which is a function of Re, Pr, λ_f, d_p and cell porosity.

As there are different phenomenon driving mass transfer, such as evaporation, mass flux due to the gradient of species concentration, species production due to chemical reactions, a generalized way to represent individual species mass source is as follows:

$$m'_{s,f,i} = (\text{Area of Mass Transfer}) \times (\text{Mass Transfer Coefficient}) \\ \times (\text{Driving Force}) \tag{2.32}$$

The total mass transfer is summation of all the species mass transfer terms.

$$m' = \sum_i m'_{s,f,i} \tag{2.33}$$

Table 2
Simulation conditions for CFD.

Variable	Value
2D grid	20 × 50
	1000 Hex elements
3D grid	20 × 20 × 50
	20,000 Hex elements
Inlet species mass fraction	
CO	0.00 [–]
CO2	0.00 [–]
N2	0.79 [–]
O2	0.21 [–]
Species mass fraction inside simulation domain	
CO	0.0 [–]
CO2	0.0 [–]
N2	0.79 [–]
O2	0.21 [–]
Time step length	0.005 s
Simulated time	20.0 s
Temperature	
Inlet	1500 K
Internal domain	1500 K
Turbulence model	$k - \epsilon$ Reynold's
	Averaged Simulation (RAS)

2.5. Computational procedure

A schematic for the CFD-DEM coupling is shown in Fig. 3. For the, XDEM and OpenFOAM libraries are linked together as a single executable. The simulations starts after running the executable. In the first step, DEM is initialized, where all the particles, walls, domain and XDEM mesh are created. After creating the mentioned assets, initial boundary conditions for the particles are applied. An initial porosity (ϵ) field is computed. Next CFD is initialized, where geometry and mesh is generated, boundary conditions on the fluid domain are applied, as well as porosity is made available to CFD solver, so that CFD solver takes into account the presence of particles from the first time step itself. But, these particles do not contribute to any heat or mass source terms of the fluid governing equations at the first time step. After all the required initializations, the time loop starts. The fluid governing equations are solved by the CFD solver developed with the assistance of OpenFOAM. The data transfer between DEM and CFD is done via direct read/write in memory. All the data is stored on the OpenFOAM mesh. After exchanging the data from CFD to DEM, the CFD data is used as boundary conditions for the particles. XDEM then solves the governing equations for the particles, and writes output fields such as porosity, momentum, heat, mass and species mass fraction source. After writing the data, the time loop proceeds to next time step ($T + dT$). In this time step, the data written by XDEM i.e various source terms, are injected in fluid governing equations. In this way the simulation continues until the specified end time T_{final}.

2.6. Simulation setup

For the simulations presented, the region of interest is only the raceway, and not the whole BF. The raceway is modeled as a 3D box of dimension 0.6 m × 0.6 m × 1.5 m. For the 2D case the cross-section dimensions remain the same (0.6 m × 1.5 m) (see Fig. 4).

The boundary conditions for the CFD and DEM are described in the Tables 2 and 3 respectively. It is assumed that the particles are preheated to 1300 K and the inlet air enters at a temperature of 1500 K. Since the primary purpose of this research is to demonstrate the effects of 3D simulations and particle discretization, the particles are spherical and of the same size to eliminate particle shape and size effects.
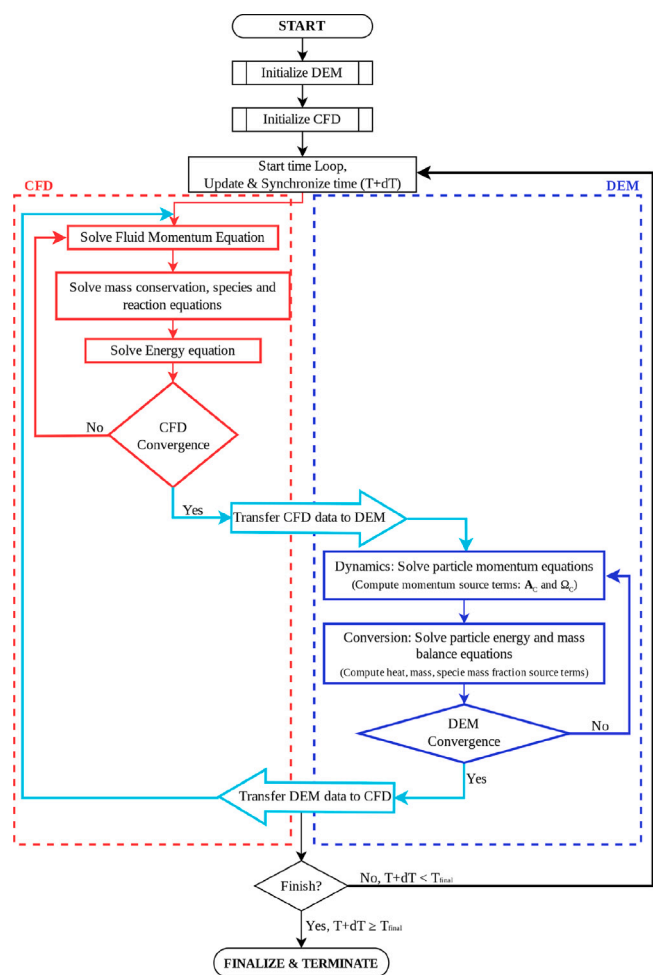
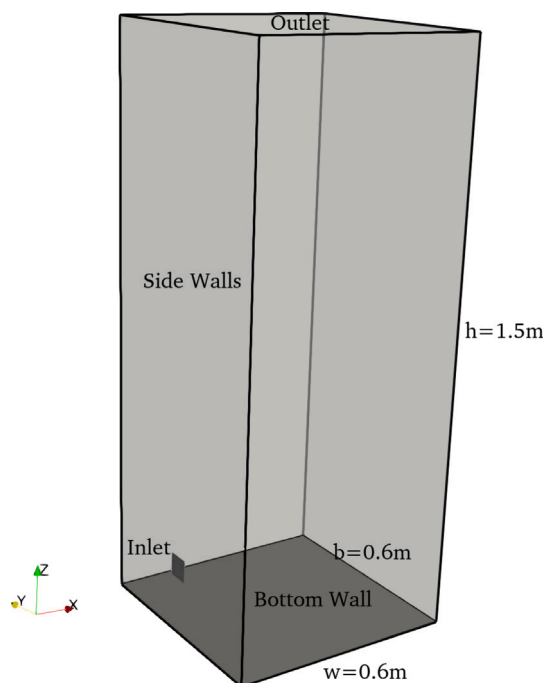**Fig. 3.** Flow chart of coupled OpenFOAM-XDEM solver showing calculation steps and exchange of data.

Fig. 4. Simulation geometry and boundaries.

Table 3
Simulation conditions for DEM.

Variable	Value
Particle shape	Spherical
Particle diameter	0.01 m
Particle density	1111.1 kg/m^3
Particle initial temperature	1300 K
Particle composition	
Char (Solid)	0.97 [–]
Light Ash (Solid)	0.03 [–]
Number of particles	10,000
Particle radial discretization	5 uniform cells
Time step length	0.005 s
Simulated time	20.0 s
Mechanical properties	
Contact model	Hertz Mindlin
Spring constant	100.0 kN/m
Viscous contact damping	2 420 000.0 N s/m
Friction coefficient	0.8 [–]
Poisson's ratio	0.45 [–]
Young's modulus	500 000.0 Pa/MPa
Thermal properties	
Thermal conductivity	0.47 W/m K
Specific heat	1500 J/kg K
Molar mass	30 [–]

3. Results and discussion

3.1. Model validation

As it was explained in Section 2, the CFD-DEM model used in this study is developed by coupling a CFD model in OpenFOAM and a particle system model in XDEM. The validations of the coupling have been presented in previous studies [25,34]. For verifying the particle-scale reaction models and gas–solid reactive interactions, the resulting gas composition from the 3D model is validated against an experimental hot model [35].

Fig. 5 shows the comparison of the simulation results for oxygen, nitrogen, and carbon monoxide against the experimental measurements. The results show that the model can predict the trend in coke combustion (oxygen consumption and carbon monoxide production) to an acceptable degree. However, there is a deviation between the predicted and measured values for oxygen and carbon monoxide which suggests and underestimated reaction rate for the coke combustion. The same level of deviation was also observed in previous studies [21,35]. This deviation is rendered as acceptable considering the harsh measurement conditions inside the furnace and thus the uncertainty associated with the measurements.

3.2. Comparison of 2D and 3D simulations of raceway

First, we propose to study the differences between 2D and 3D simulations of the raceway. The 2D model is presented in a previous work [34]. As mentioned before, there have already been a lot of efforts in developing 2D models of the raceway and the BF. Simulations in 2D have the advantage of lower computational cost, but they come at the expense of numerical accuracy. Undoubtedly there should be a reasonable trade-off between the advantages and disadvantages. In the present work, 2D and 3D simulations are compared and the results reveal a significant discrepancy in raceway behavior. In order to make a valid comparison, the 2D and 3D cases were similar in size and mesh in the *x* and z direction. There are also similar initial conditions, including packed bed height and particle size.

Fig. 6 shows the comparison of the raceway cavity in 2D and 3D simulations of the dynamics of a BF raceway. It can be observed that in 2D, the raceway cavity has larger dimensions compared to the 3D results. The height and width of the raceway in the 2D case are
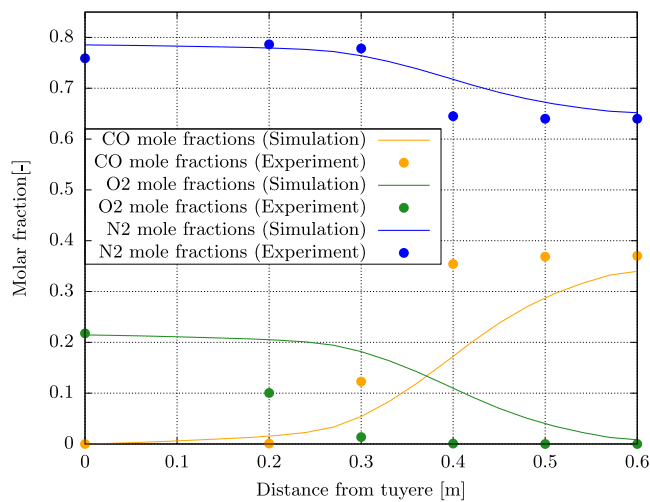
Fig. 5. Comparison of the measured and predicted gas compositions along the central axis of the tuyere.
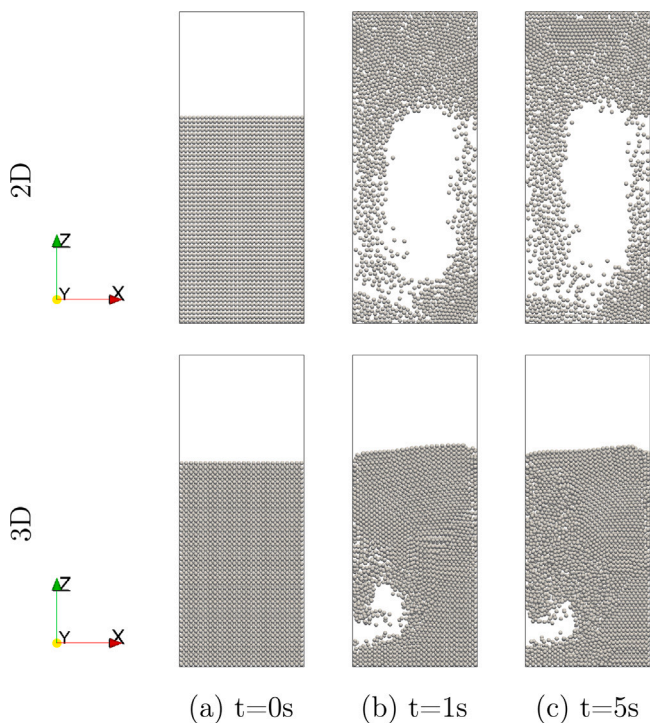

(a) t=0s   (b) t=1s   (c) t=5s

Fig. 6. The 2D and 3D dynamics simulation of a blast furnace raceway at three different time steps. The 3D results are slices from the 3D packed bed cut between two XZ planes on the two sides of the inlet.

respectively 100 cm and 38 cm, while in 3D they are respectively 30 cm and 12 cm. This notable discrepancy between the 2D and the 3D simulations can be explained by the fact that in 3D, the momentum of the inlet flow is partly consumed to expand the raceway in the third direction, depth (which reaches up to 24 cm). Whereas in 2D simulation the momentum of the inlet air is wholly saved to expanding the raceway height and width, thus resulting in an unjustifiably large raceway. The result is that in the 2D simulation, the packed bed is expanded to fill the whole available domain whereas in reality the top of the packed bed is just raised a fraction of the packed bed height. This behavior can be observed in the previous study as well [21]. This phenomenon can be confronted by defining different initial or boundary conditions to constrain the packed bed height or fill the

whole domain from the beginning but nevertheless, it would not change the fact that the dynamics of the packed bed and the raceway are misrepresented.

Moreover, the implicit assumption made for the 2D model by itself leads to a significant gap between the model and actual physics. The 2D simulation of the raceway assumes a symmetrical placement of the raceway in the BF. For 2D simulation to represent the real BF raceway, either the BF should be a thin slice with two raceways on the opposite sides, which is naturally far from the reality, where we have a cylindrical furnace with multiple injection inlets located on the periphery; or, the inlet of the raceway should be an open slit covering the periphery which would lead to a torus raceway in the whole furnace. None of these two cases mimic the actual physical geometry to a good approximation. Due to such observations, the previous studies have noted [13] that there should be special boundary conditions defined on the domain for the 2D or quasi-3D model to represent the physics better.

However, in a 3D simulation, the actual physics of the problem is represented more accurately. As is presented in the following sections, the raceway enlargement is more confined and the packed bed movement is very limited compared to a 2D simulation. Therefore, the significant difference between the two cases led to the conclusion that 3D simulations, despite their computational costs, provide a much more reliable insight into the physics of the raceway. Additionally, with the increasing trend in computational power and thanks to parallelization, 3D simulations are becoming more affordable.

3.3. Typical transport phenomena of the raceway

Fig. 7 provides a series of snapshots from the 3D simulation of a raceway section in an operating BF. The pictures depict the raceway formation as a hot air blast is injected horizontally into the furnace via the tuyeres. Following the blast, the raceway forms in the early time steps. It first penetrates the packed bed to the maximum possible depth in a horizontal direction which is approximately 24 cm, then adopts an upward anti-clockwise direction to develop further in height and eventually reach a maximum height of 33 cm from the bottom of the furnace. As can be seen in the figures, by the time of 20 s the raceway has already adopted a respectively steady shape and dimensions. Fig. 8 shows the penetration profiles of the raceway through time in X-direction (depth), Z-direction (height) and Y-direction (width). This plot supports the observations in Fig. 7, by showing that the raceway dimensions achieve stability in all directions by 20 s, despite abrupt fluctuations in the beginning. However, the width of the raceway shows less stability because it is comparatively confined by the walls.

As a more clear depiction of the 3D case, Fig. 9 shows the location of the raceway and the gas flow streamlines that start from the inlet and spread all through the raceway. As can be seen in the figure, the gas flow has a high velocity inside the raceway (more than 50 m/s) and as it penetrates into the packed bed, loses its momentum and its velocity decreases drastically.

3.4. Heat and mass distribution in the packed bed

Fig. 10 demonstrates the particles and their respective temperature at three different time steps on horizontal and vertical slices. These horizontal and vertical slices are cut between two XY and XZ planes respectively located at Z = 0.15 cm, Z = 0.21 cm, and Y = 0.27 cm, Y = 0.33 cm. As can be seen in the XZ slices (subfigures a–c), the packed bed has increased in height because of the minor fluidization caused by the flow inside the raceway. The packed bed's top surface shows a downward slope from right to left, representing a general anti-clockwise flow flowing through the packed bed.

The particles preheated to an initial temperature of 1300 K. Fig. 10 shows that as the raceway forms, the temperature of particles around the ring-type zone rises. The ring-type zone is the boundary of the
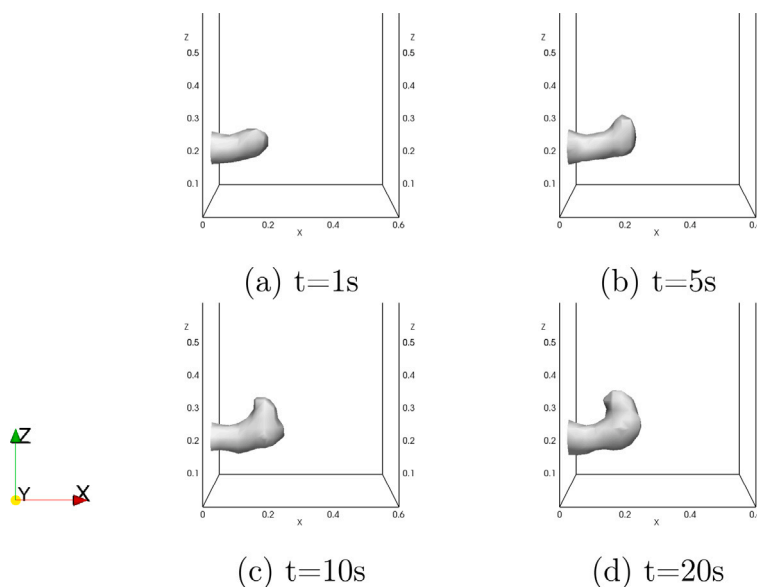
(a) t=1s

(b) t=5s

(c) t=10s

(d) t=20s

Fig. 7. Topological evolution of the raceway cavity at different time steps in the 3D simulation of a BF raceway with a blast velocity of 200 m/s.
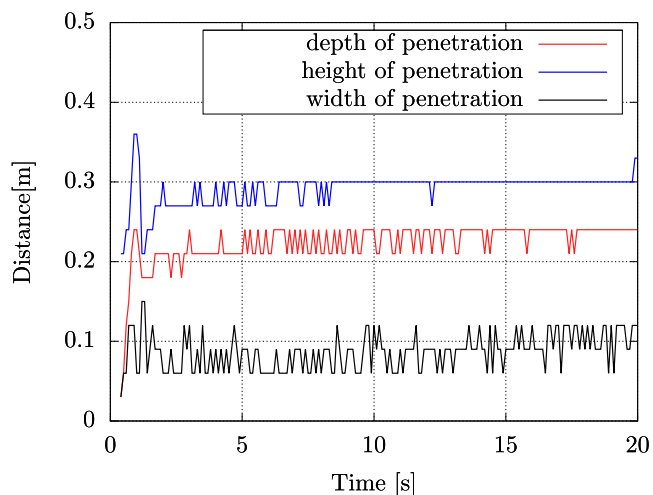

Fig. 8. Temporal variation in depth (starting from tuyere tip in the direction of inlet flow, i.e. inlet central line), height (starting from the bottom of the furnace in the positive z-direction) and width (starting from inlet center line in the positive y-direction) of the raceway cavity calculated based on the porosity isoline of 0.7.
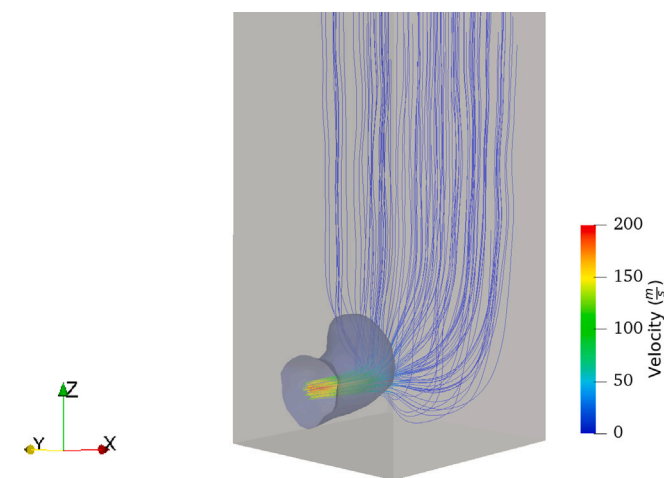

Fig. 9. Streamlines of the flow passing through raceway for the 3D case with an inlet velocity of 200 m/s. The streamlines are colored by the flow velocity. (For interpretation of the references to color in this figure legend, the reader is referred to the web version of this article.)

raceway and the location where the incoming air meets the coke particles. The oxygen concentration in this zone is high, causing a high rate of the exothermic oxidation reaction with coke. Heat is produced at a faster rate when the reaction rate is higher, therefore the temperature is raised faster in the areas close to the ring-type zone.

The distribution of O_2 and CO at t = 0.1 s, t = 1 s and t = 20 s can be seen in Fig. 11. In the initial time step (t = 0 s) the mass fraction of both O_2 and CO is zero and only Nitrogen (N_2) is present(which is not shown here for the sake of brevity). As the simulation process starts, O_2 is blasted into the furnace and CO is produced. It can be observed that the raceway region is the source of O_2 and distributes it around the packed bed. This explains the correspondence of the O_2 distribution with the raceway shape. However this correspondence is very rough because some O_2 distributes into the packed bed via diffusion and convection and therefore go beyond the raceway perimeter. The O_2 concentration is maximum in the raceway and zero beyond the ring-type zone because the coke particles in the zone consume the O_2 and produce CO. Consequently, due to the outward flow direction around

the raceway, CO transports away from the raceway. As a result, CO concentrations inside the raceway are lower than outside.

3.5. Influence of blast flow rate

Inlet velocity is a physical parameter that can be manipulated to achieve the desired outcome in the raceway. It directly affects the size of the raceway and thus the distribution of temperature and gas species. In this study, three test cases with inlet velocities of 180 m/s, 200 m/s, and 220 m/s are used to examine the effects of inlet velocity on raceway transport phenomena.

In all the cases, the initial inlet velocity is 10 m/s and it increases linearly with time, up to the desired inlet velocity (180, 200, or 220 m/s) at t = 0.5 s. This gradual velocity increase was done both for the sake of stability and imitating the actual process. As can be seen in Fig. 12, increasing the inlet velocity results in a larger raceway, thus pushing the ring-type zone outward. As the raceway approaches proximate stability, the volumes of the raceway cavity for 180 m/s, 200 m/s, and 220 m/s are respectively 4.24, 4.72 and 6.56 cubic decimeters. These
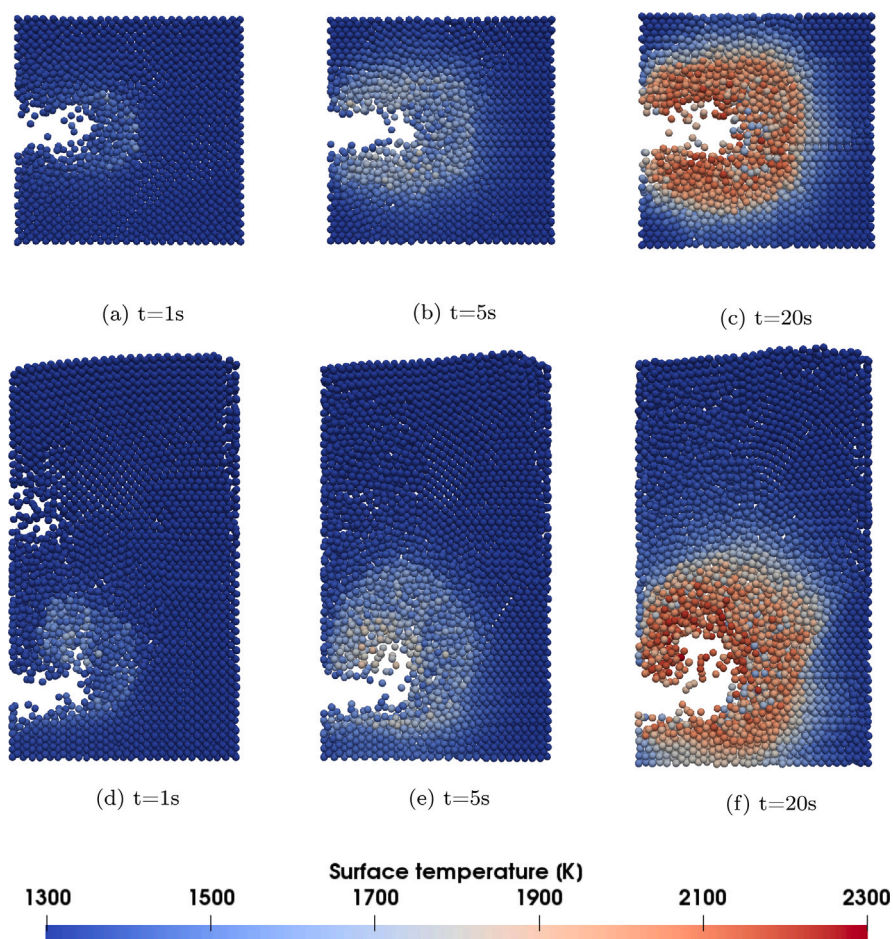
Fig. 10. Spatial distributions of coke particles in the raceway packed bed at different time steps in a horizontal slice cut from the 3D packed bad, between two XY planes on the opposite sides of the inlet (a,b,c) and a vertical cut between two XZ planes on the opposite sides of the inlet (d,e,f). Particles are colored by the surface temperature of the particles. (For interpretation of the references to color in this figure legend, the reader is referred to the web version of this article.)
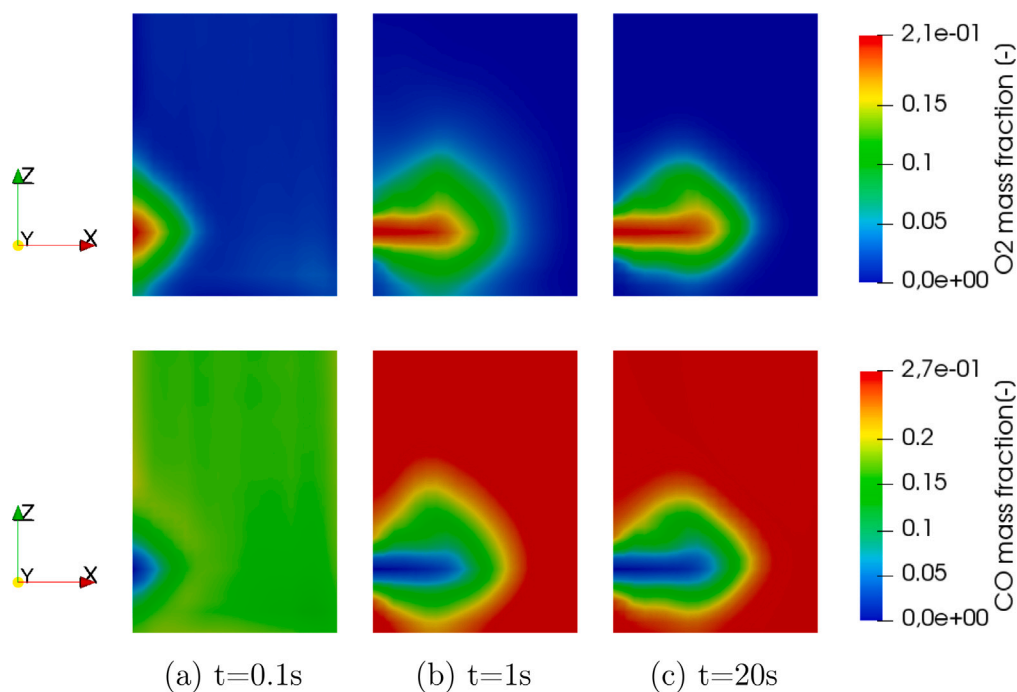

Fig. 11. O_2 and CO mass fraction distribution in the gas (CFD) at different time steps of the 3D simulation on an XZ slice located on Y = 0.3 m which passes the inlet.
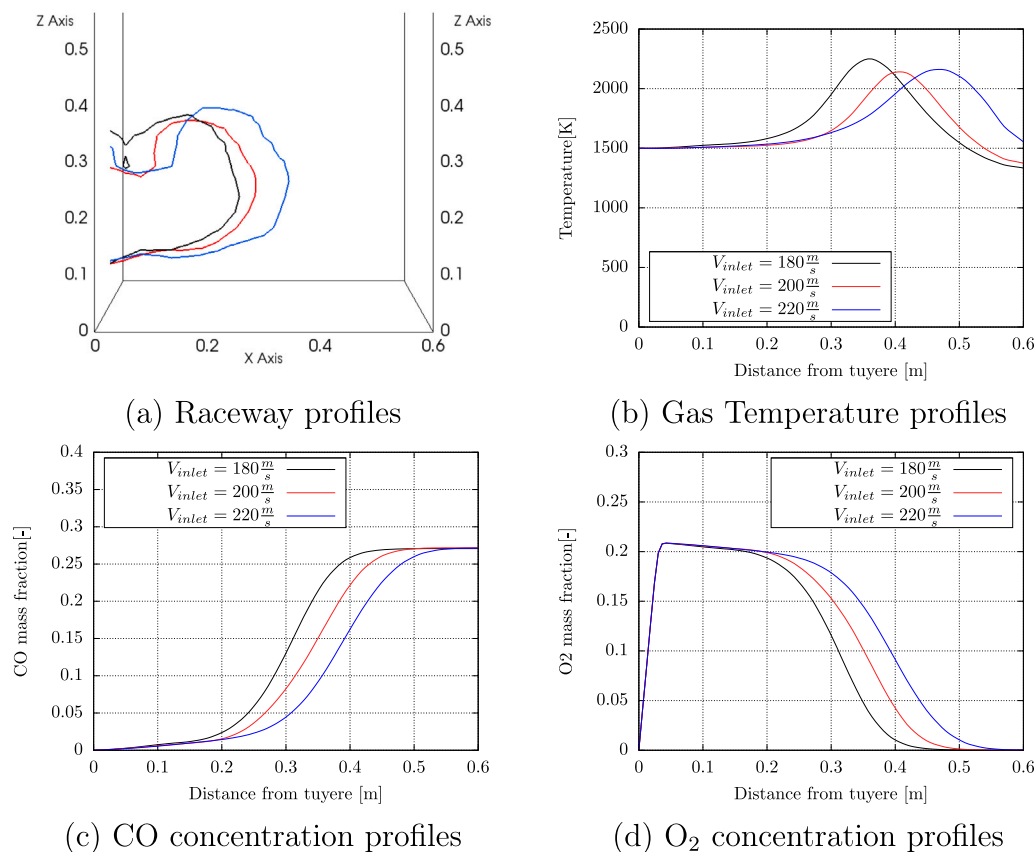
(a) Raceway profiles

(b) Gas Temperature profiles

(c) CO concentration profiles

(d) O_2 concentration profiles

Fig. 12. Comparison of raceway profile, temperature, CO concentration and O_2 concentration along the horizontal line from the tuyere tip for three different velocities 180 m/s (black), 200 m/s (red) and 220 m/s (blue). (For interpretation of the references to color in this figure legend, the reader is referred to the web version of this article.)

values are calculated based on considering the raceway as the region with a porosity equal to or larger than 0.7.

Fig. 12b shows the variation of temperature along the horizontal line starting from the tuyere tip. In all three cases, somewhere in the middle of the horizontal line, there is a temperature peak. The high combustion rate of the particles and the resulting heat causes the temperature to rise. Based on the raceway profiles in Fig. 12a these peaks occur in the ring-type zone which is located just outside the raceway perimeter. The same behavior can be observed in O_2 and CO concentration profiles in Fig. 12. As is expected, at the ring-type zone (for instance, between 0.2 m–0.4 m for 180 m/s case), there is a rapid consumption of oxygen, concurrent with the formation of carbon monoxide, which reaches its maximum concentration at the end of the probe line. This consistency of the temperature and concentration profiles with the raceway profile can be observed for all three inlet velocities. However, as the blast inlet velocity is increased, the ring-type zone is pushed further outward therefore the temperature peak and correspondingly the concentration profiles' inclination, occur at a further distance from the tuyere tip.

3.6. Heat and mass distribution within the particles

As described in Section 2.1.2, the DEM model used in this study considers discretized particles. Therefore the heat and mass distributions inside the particles are considered, featuring the internal gradients of temperature and species concentration within the particles.

Fig. 13 compares the results between a case with 1-cell particles and a case with 5-cell particles to demonstrate the significance of particle discretization. The primary difference between a 1-cell and a 5-cell particle is that in the 5-cell case there is a gradient of species and temperature within the particle. Coke combustion is driven by oxygen

which diffuses into the particle from the ambient gas. Therefore the oxygen concentration has a profile within the particle, decreasing from the surface to the center. The available oxygen concentration determines the rate of coke combustion. Therefore the combustion reaction rate will have a negative gradient from the surface to the center, resulting in more heat generation (due to the exothermic reaction of coke combustion) in the cells near to the surface. Since the particle surface temperature is higher in the 5-cell case, there is a stronger heat convection with the surrounding ambient gas and the gas is thus hotter. This anticipation is clearly demonstrated by Fig. 13(b). The case with 5-cell particles shows a higher gas temperature peak in the ring-type zone. This higher gas temperature creates a higher pressure inside the raceway which pushes the raceway ceiling upward (as there is less resistance to vertical expansion compared to horizontal expansion which is limited by the right wall). This explains the larger raceway cavity for 5-cell particles as illustrated in Fig. 13(a).

However, it is important to note that although in the 5-cell case there is a gradient in reaction rate through the cell, the average reaction rate, or in other words the coke and oxygen consumption is almost the same in the two cases. Figs. 13(c) and (d) show respectively CO and O_2 concentration along the horizontal line from the tuyere tip. It can be observed that there is almost no difference between the two cases in O_2 consumption and CO production.

The aforementioned gradient of temperature can be significant in some particles that are subject to higher O_2 concentration. Fig. 14 shows the temperature distribution over the particle radius for two different particles located at different points in the packed bed. Both of these two cases include particles with 20 cells so that this gradient is expressed more clearly. One is inside the ring-type zone, undergoing higher reaction rates and higher temperatures. The other particle, particularly in the second half of simulation, experiences lower temperatures, suggesting that it evaded being trapped in the ring-type zone
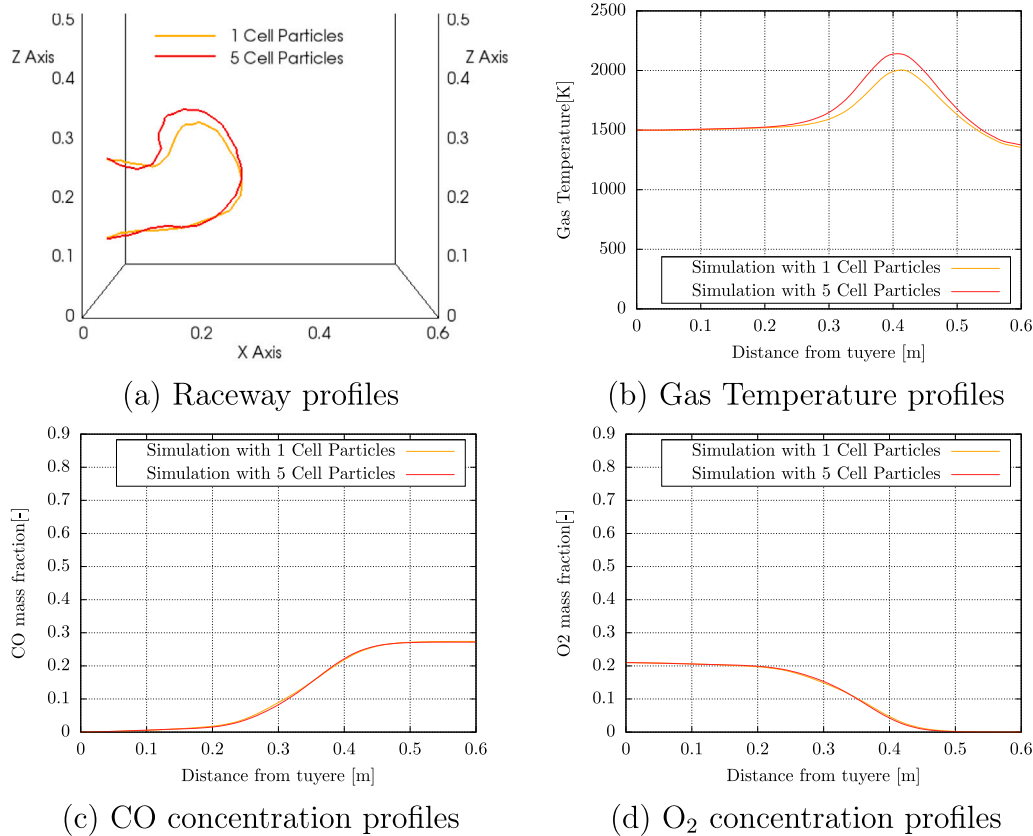
(a) Raceway profiles

(b) Gas Temperature profiles

(c) CO concentration profiles

(d) O$_2$ concentration profiles

Fig. 13. Comparison of raceway profile, gas temperature, gas CO concentration and gas O$_2$ concentration along the horizontal line from the tuyere tip for two cases: particles with one internal cell and thus no discretization (Orange) and particles with 5 cells (Red). (For interpretation of the references to color in this figure legend, the reader is referred to the web version of this article.)
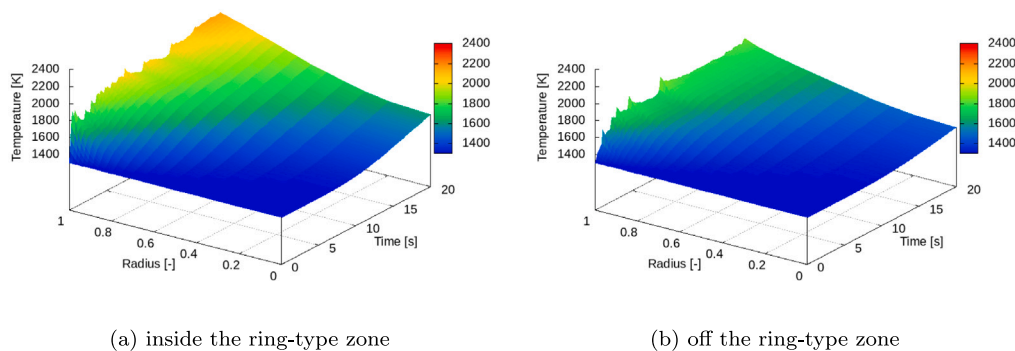

(a) inside the ring-type zone

(b) off the ring-type zone

Fig. 14. Temporal and spatial distribution of temperature in two coke particles: (a) one, positioned inside the ring-type zone and (b) the other, further away from the ring-type zone.

and maintained a position where heat loss and heat gain by the particle are in equilibrium.

The figures demonstrate the particle discretization which is non-uniform as it was explained in Section 2.1.2. The cell adjacent to the particle surface adopts a minimum size and towards the center of the particle the cell size increases according to a geometric progression. It can be observed that in both cases there is a high gradient of temperature near the surface and this gradient increases over time, because of the low conductivity of coke. This sharp gradient would not be captured in a particle with no discretization [18,20]. Therefore such models in which the whole particle is considered as a single element with a uniform temperature all over it, incorporate a rough temperature

in the Arrhenius model and thus underestimate the reaction rates at the surface of the particle. As demonstrated in previous sections, in an application such as a BF where there is a complex interdependency between the heat transfer, reactions and the dynamics of the system, such gaps in the model will introduce noticeable and unacceptable errors.

4. Conclusion

A CFD-DEM model was developed to analyze the raceway transport phenomena in an iron-making blast furnace. The study proposed the significance of simulating the raceway in 3D. Based on the provided

results, it was argued that the 2D model, due to the implicit assumptions associated with it, overestimates the raceway size. Therefore the 3D model was used to simulate the raceway and analyze the dynamical evolution of the raceway, combustion of the coke particles, and heat and species distribution in the gas flow.

It was shown that the coke combustion rate is the highest in the periphery of the raceway, known as the ring-type zone. Therefore almost all of the incoming oxygen is consumed near the ring-type zone and the particles in this region experience the highest temperatures. The discretization of the particles made it possible to analyze the heat distribution within the particles. It was shown that for the particles exposed to high oxygen concentration and high combustion rate, the surface of the particle is subjected to a relatively high temperature gradient. Therefore, in a blast furnace where thermal conductivity of coke particles is low but temperature levels are high, using a DEM model with discretized particles is an effective strategy for preventing the underestimation of particle temperatures.

The influence of the gas inlet velocity was also investigated. It was shown that higher inlet velocity results in larger raceway cavities and more penetration into the path of the packed bed. However, the temperature ranges of the raceway and reaction rates do not follow a clear correlation with the inlet blast flow rate. These findings offer insight into the complex correlations between the dynamics and thermodynamics of the raceway.

CRediT authorship contribution statement

Navid Aminnia: Methodology, Visualization, Investigation, Writing. **Prasad Adhav:** Methodology, Visualization, Investigation, Writing. **Fateme Darlik:** Investigation, Data curation, Writing. **Muhammad Mashhood:** Validation, Conceptualization, Reviewing and editing. **Sina Hassanzadeh Saraei:** Validation, Conceptualization, Reviewing and editing. **Xavier Besseron:** Software, Methodology, Supervision, Reviewing and editing. **Bernhard Peters:** Conceptualization, Software, Methodology, Supervision.

Declaration of competing interest

The authors declare the following financial interests/personal relationships which may be considered as potential competing interests: Navid Aminnia reports financial support was provided by Luxembourg National Research Fund (FNR). Sina Hassanzadeh Saraei reports a relationship with Luxembourg National Research Fund (FNR) that includes: funding grants.

Data availability

Data will be made available on request.

Acknowledgment

References

[1] Zhang Qi, Xu Jin, Wang Yujie, Hasanbeigi Ali, Zhang Wei, Lu Hongyou, Arens Marlene. Comprehensive assessment of energy conservation and CO2 emissions mitigation in China's iron and steel industry based on dynamic material flows. Appl Energy 2018;209:251–65.

[2] de Castro Jose Adilson, Takano Cyro, Yagi Jun-ichiro. A theoretical study using the multiphase numerical simulation technique for effective use of H2 as blast furnaces fuel. J Mater Res Technol 2017;6(3):258–70.

[3] Chunbao Charles Xu, Cang Da-qiang. A brief overview of low CO2 emission technologies for iron and steel making. J Iron Steel Res Int 2010;17(3):1–7.

[4] Sun Wenqiang, Wang Qiang, Zhou Yue, Wu Jianzhong. Material and energy flows of the iron and steel industry: Status quo, challenges and perspectives. Appl Energy 2020;268:114946.

[5] Shen Yansong, Guo Baoyu, Chew Sheng, Austin Peter, Yu Aibing. Three-dimensional modeling of flow and thermochemical behavior in a blast furnace. Metall Mater Trans B 2015;46(1):432–48.

[6] Dong S, Paterson N, Kazarian SG, Dugwell DR, Kandiyoti R. Characterization of tuyere-level core-drill coke samples from blast furnace operation. Energy & Fuels 2007;21(6):3446–54.

[7] Matsui Yoshiyuki, Yamaguchi Yasuhiro, Sawayama Muneyoshi, Kitano Shinji, Nagai Nobuyuki, Imai Takashi. Analyses on blast furnace raceway formation by micro wave reflection gunned through tuyere. ISIJ Int 2005;45(10):1432–8.

[8] Sastry GSSRK, Gupta GS, Lahiri AK. Cold model study of raceway under mixed particle conditions. Ironmak Steelmak 2003;30(1):61–5.

[9] Sastry GSSRK. Void formation and breaking in a packed bed. ISIJ Int 2003;43(2):153–60.

[10] Zhang Ruixuan, Cheng Yuxin, Li Yan, Zhou Dongdong, Cheng Shusen. Image-based flame detection and combustion analysis for blast furnace raceway. IEEE Trans Instrum Meas 2019;68(4):1120–31.

[11] Mondal SS, Som SK, Dash SK. Numerical predictions on the influences of the air blast velocity, initial bed porosity and bed height on the shape and size of raceway zone in a blast furnace. J Phys D: Appl Phys 2005;38(8):1301.

[12] Qiu Xiaoping, Wang Limin, Yang Ning, Li Jinghai. A simplified two-fluid model coupled with EMMS drag for gas-solid flows. Powder Technol 2017;314:299–314.

[13] Yang WJ, Zhou ZY, Yu AB. Discrete particle simulation of solid flow in a three-dimensional blast furnace sector model. Chem Eng J 2015;278:339–52.

[14] Xu BH, Feng YQ, Yu AB, Chew SJ, Zulli P. A numerical and experimental study of the gas-solid flow in a fluid bed reactor. Powder Handl Process 2001;13(1):71–6.

[15] Feng Yu-Qing, Pinson David, Yu Ai-Bing, Chew Shen J, Zulli Paul. Numerical study of gas-solid flow in the raceway of a blast furnace. Steel Res Int 2003;74(9):523–30.

[16] Yuu Shinichi, Umekage Toshihiko, Kadowaki Masatomo. Numerical simulation of particle and air velocity fields in raceway in model blast furnace and comparison with experimental data (cold model). ISIJ Int 2010;50(8):1107–16.

[17] Hilton JE, Cleary PW. Raceway formation in laterally gas-driven particle beds. Chem Eng Sci 2012;80:306–16.

[18] Wang Shuai, Shen Yansong. CFD-DEM modelling of raceway dynamics and coke combustion in an ironmaking blast furnace. Fuel 2021;302:121167.

[19] Miao Zhen, Zhou Zongyan, Yu AB, Shen Yansong. CFD-DEM simulation of raceway formation in an ironmaking blast furnace. Powder Technol 2017;314:542–9.

[20] Cui Jiaxin, Hou Qinfu, Shen Yansong. CFD-DEM study of coke combustion in the raceway cavity of an ironmaking blast furnace. Powder Technol 2020;362:539–49.

[21] Dianyu E, Zhou Peng, Guo Suya, Zeng Jia, Xu Qiang, Guo Liejin, Hou Qinfu, Yu Aibing. Particle-scale study of coke combustion in the raceway of an ironmaking blast furnace. Fuel 2022;311:122490.

[22] Zhuo Yuting, Hu Zhongjie, Shen Yansong. CFD study of hydrogen injection through tuyeres into ironmaking blast furnaces. Fuel 2021;302:120804.

[23] Li Tao, Wang Guangwei, Zhou Heng, Ning Xiaojun, Zhang Cuiliu. Numerical simulation study on the effects of co-injection of pulverized coal and hydrochar into the blast furnace. Sustainability 2022;14(8):4407.

[24] Okosun Tyamo, Nielson Samuel, Zhou Chenn. Blast furnace hydrogen injection: Investigating impacts and feasibility with computational fluid dynamics. JOM 2022;74(4):1521–32.

[25] Peters Bernhard, Baniasadi Maryam, Baniasadi Mehdi, Besseron Xavier, Donoso Alvaro Estupinan, Mohseni Mohammad, Pozzetti Gabriele. XDEM multi-physics and multi-scale simulation technology: Review of DEM–CFD coupling, methodology and engineering applications. Particuology 2019;44:176–93.

[26] Baniasadi Mehdi, Baniasadi Maryam, Peters Bernhard. Coupled CFD-DEM with heat and mass transfer to investigate the melting of a granular packed bed. Chem Eng Sci 2018;178:136–45.

[27] Peters Bernhard. Thermal conversion of solid fuels. International series on developments in heat transfer, vol. 15 15, Southampton: WIT Press; 2003.

[28] Rhead Thomas Fred Eric, Wheeler Richard Vernon. CCXXVI.—The effect of temperature on the equilibrium 2CO⇌CO 2+ C. J Chem Soc Trans 1910;97:2178–89.

[29] Zhao Tao. Coupled DEM-CFD analyses of landslide-induced debris flows. Springer; 2017.

[30] Gidaspow Dimitri. Multiphase flow and fluidization: Continuum and kinetic theory descriptions. Academic Press; 1994.

[31] Wen CY, Yu YH. Mechanics of fluidization. In: The chemical engineering progress symposium series, Vol. 162. 1966, p. 100–11.

[32] Ergun Sabri, Orning Ao Ao. Fluid flow through randomly packed columns and fluidized beds. Ind Eng Chem 1949;41(6):1179–84.

[33] Xiao Heng, Sun Jin. Algorithms in a robust hybrid CFD-DEM solver for particle-laden flows. Commun Comput Phys 2011;9(2):297–323.

[34] Santana Edder Rabadan, Pozzetti Gabriele, Peters Bernhard. Application of a dual-grid multiscale CFD-DEM coupling method to model the raceway dynamics in packed bed reactors. Chem Eng Sci 2019;205:46–57.

[35] Nogami Hiroshi, Yamaoka Hideyuki, Takatani Kouji. Raceway design for the innovative blast furnace. ISIJ Int 2004;44(12):2150–8.